Received: 12 January 2024 | Revised: 27 May 2024 | Accepted: 18 June 2024

DOI: 10.1111/psyp.14641

PSYCHOPHYSIOLOGY SPR WILEY

ORIGINAL ARTICLE

Cortical and subcortical brain networks predict prevailing heart rate

Amy Isabella Sentis[1,2] | **Javier Rasero**[2,3,4] | **Peter J. Gianaros**[2,5] | **Timothy D. Verstynen**[2,3,6]

[1]Medical Scientist Training Program, University of Pittsburgh and Carnegie Mellon University, Pittsburgh, Pennsylvania, USA

[2]Carnegie Mellon Neuroscience Institute, University of Pittsburgh and Carnegie Mellon University, Pittsburgh, Pennsylvania, USA

[3]Department of Psychology, Carnegie Mellon University, Pittsburgh, Pennsylvania, USA

[4]School of Data Science, University of Virginia, Charlottesville, Virginia, USA

[5]Department of Psychology, University of Pittsburgh, Pittsburgh, Pennsylvania, USA

[6]Biomedical Engineering, Carnegie Mellon University, Pittsburgh, Pennsylvania, USA

Correspondence
Timothy D. Verstynen, Department of Psychology, Carnegie Mellon University, 342E Baker Hall, 5000 Forbes Avenue, Pittsburgh, PA 15213, USA.
Email: timothyv@andrew.cmu.edu

Funding information
National Institutes of Health, Grant/Award Number: T32GM008208-29; National Heart, Lung, and Blood Institute, Grant/Award Number: P01HL040962 and R01089850

Abstract

Resting heart rate may confer risk for cardiovascular disease (CVD) and other adverse cardiovascular events. While the brainstem's autonomic control over heart rate is well established, less is known about the regulatory role of higher level cortical and subcortical brain regions, especially in humans. This study sought to characterize the brain networks that predict variation in prevailing heart rate in otherwise healthy adults. We used machine learning approaches designed for complex, high-dimensional data sets, to predict variation in instantaneous heart period (the inter-heartbeat-interval) from whole-brain hemodynamic signals measured by fMRI. Task-based and resting-state fMRI, as well as peripheral physiological recordings, were taken from two data sets that included extensive repeated measurements within individuals. Our models reliably predicted instantaneous heart period from whole-brain fMRI data both within and across individuals, with prediction accuracies being highest when measured within-participants. We found that a network of cortical and subcortical brain regions, many linked to visceral motor and visceral sensory processes, were reliable predictors of variation in heart period. This adds to evidence on brain–heart interactions and constitutes an incremental step toward developing clinically applicable biomarkers of brain contributions to CVD risk.

KEYWORDS
cardiovascular disease risk, fMRI, heart rate, machine learning

Peter J. Gianaros and Timothy D. Verstynen co-senior authors.

1 | INTRODUCTION

Resting heart rate (HR) is not only a predictor of all-cause mortality, but is also a risk factor for cardiovascular disease in individuals with and without preexisting cardiovascular disease (CVD; [Böhm et al., 2015; Fox et al., 2007; Palatini, 2007; Perret-Guillaume et al., 2009]). High resting HR has been associated with progression of coronary artery atherosclerosis and the occurrence of myocardial ischemia and arrhythmias, and is implicated in left ventricular dysfunction (Boudoulas et al., 2015; Custodis et al., 2010; Fox et al., 2007; Huikuri et al., 1999; Palatini, 2007; Perret-Guillaume et al., 2009). Conversely, reduction of resting HR has long been associated with the prevention of activity-related angina and ischemia (Fox et al., 2007). High resting HR is often comorbid in individuals with other cardiometabolic risk factors, including hypertension, high blood lipid and glucose levels, and overweight or high BMI (Fox et al., 2007; Palatini & Julius, 1999). A large-scale, long-term follow-up epidemiological study found high resting HR to be a risk factor for all-cause mortality, as well as death from acute myocardial infarction, after adjusting for possible confounds such as age, BMI, systolic BP, diabetes diagnosis, and level of physical activity (Fox et al., 2007; Jouven et al., 2005).

Evidence from animal studies and human lesion studies have shown that HR is under autonomic control, with cell groups of the brainstem exerting proximal regulation (Critchley et al., 2003; Guyenet & Koshiya, 1995; Ongür & Price, 2000; Thornton et al., 2002; Verberne & Owens, 1998). This brain–heart link has been more recently validated by human neuroimaging studies (Critchley, 2005; Critchley et al., 2003). This link also extends further "up" the brain, to evolutionarily newer brain regions like the telencephelon (i.e., neocortex), which seems to play a role in the behavioral and psychological modulation of HR (Ginty et al., 2017). During psychologically stressful contexts, for example, several cortical areas appear to exert direct and indirect cardiac control via the autonomic nervous system (Brotman et al., 2007; Carrive, 2006; Kivimäki & Steptoe, 2018; Steptoe & Kivimäki, 2013). Indeed, the role of behavioral and psychological processes in modulating cardiac function provides a particularly clear indication of the role that cortical function has on HR (Dar et al., 2019; Eisenbarth et al., 2016; Ginty et al., 2017; Kraynak et al., 2018; Tawakol et al., 2019).

Here, we sought to characterize the brain networks that predict variation in prevailing HR within healthy individuals. To do so, we used machine learning approaches designed for complex and high-dimensional data sets to predict instantaneous heart period (the inter-heartbeat-interval) from temporal variation in whole-brain hemodynamic signals measured using fMRI. Here, we evaluated two hypotheses. First, we evaluated whether it is possible to reliably predict modulation of heart period from hemodynamic responses in the brain *within individuals*. Second, we looked at whether the brain regions that are most important for this prediction would encompass part or all of brain areas implicated in visceral motor and visceral sensory processes (Zhang et al., 2023).

2 | METHODS

2.1 | Human QA dataset

2.1.1 | Participants

Neuroimaging and cardiovascular data were collected from one healthy participant (white male in his 40s, BMI 23.1) at 14 repeated scan sessions over a period of 20 weeks at the CMU-Pitt BRIDGE Center (RRID:SCR 023356). The participant did not perform any strenuous exercise or consume any caffeine, nicotine, or alcohol prior to scanning sessions. Three fMRI scans with concurrent electrocardiogram (ECG) and pneumatic belt physiological signals were collected at each session, along with a structural MRI scan, for a total of 42 runs. The participant provided informed consent to complete the study, which was approved by the Carnegie Mellon University (Pittsburgh, PA) Institutional Review Board.

2.1.2 | MRI data acquisition and processing

Acquisition

Functional blood oxygenation level-dependent images were collected on a Siemens Prisma 3 Tesla scanner, equipped with a 64-channel head coil. Over an 8 min 54 s period with eyes open, resting-state and task-dependent functional images were acquired with acquisition parameters as follows: 2 mm iso voxels, FOV = 212 × 212 mm, TR = 1500 ms, TE = 30 ms, FA = 79°, and multiband acceleration factor = 4. Sixty-eight interleaved slices (2 mm thickness, no gap) in the ascending direction were obtained for each of 353 volumes (with three initial volumes discarded to allow for magnetic equilibration). Task-dependent functional images were collected while the participant played the game cooperative space fortress, teaming with a variety of artificial intelligence co-players (Dimov et al., 2020). T1-weighted neuroanatomical magnetization prepared rapid gradient echo (MPRAGE) images were collected in 208 slices (1 mm thickness, no gap) over a 7 min 58 s period with acquisition parameters as follows: 1 mm iso voxels, FOV = 256 × 256 mm, TR = 2300 ms, TE = 2.03 ms, TI = 900 ms, and FA = 9°.

Preprocessing

Preprocessing was performed using fMRIPrep version 20.2.7 ([Esteban et al., 2019]; RRID:SCR_016216). Eight T1-weighted images collected across the 14 sessions were combined into one average T1-weighted reference map. Anatomical and functional images were normalized to the ICBM 152 Nonlinear Asymmetrical template version 2009c ([Fonov et al., 2009], RRID:SCR_008796; TemplateFlow ID: MNI152NLin2009cAsym) to facilitate between-participant and between-data set comparisons.

Gray matter (GM) mask

Using the GM tissue probability reference image in MNI152NLin2009cAsym standard space output from fMRIPrep, we generated a binary mask (thresholded at probability >0.2) to limit our analysis to GM voxels.

2.1.3 | Heart period from ECG

ECG data were collected concurrently during functional MRI (fMRI) scans at a sampling rate of 400 Hz using the Siemens physiological monitoring unit's standard configuration. Data were processed using *niphlem* (https://coaxlab.github.io/niphlem/) and included the following steps: (1) subtraction of ground ECG channel from remaining channels, (2) demean channels, (3) bandpass filtering (0.6–5 Hz), and (4) average channels. Signal peaks were identified (specifically, the R peaks within the QRS waveform) with subsequent detection of artifacts through two one-sided Grubb's tests for outliers and correction.

Heart rate is derived by taking the inverse of heart period (the interbeat interval, or the time between ECG signal peaks), which is a nonlinear transformation. It is known that heart rate behaves nonlinearly in many contexts, especially with respect to underlying autonomic input, (Berntson et al., 1995; de Geus et al., 2019). While both measures are controlled in part by autonomic inputs, there exists a more linear relationship between autonomic control and heart period, when compared to heart rate (Berntson et al., 1995; de Geus et al., 2019). Thus, heart rate and heart period are not interchangeable with respect to autonomic control. Additionally, the distribution of heart period has been demonstrated to be more statistically normal when compared to that of heart rate (Jennings et al., 1974). For these reasons, we used heart period as our target variable. The processed vectors of heart rate and period were then downsampled to match the fMRI TR, to allow for a one-to-one correspondence of our predictor (i.e., voxels) and response variables (e.g., heart period) for our prediction models (see also, [Eisenbarth et al., 2016; Wager et al., 2009]).

2.1.4 | Analysis

Figure 1 shows the structure of our analysis pipeline, which involves three stages: preprocessing, denoising, and model analysis. Preprocessing was performed using fMRIPrep and *niphlem* for the fMRI and physiological data, respectively, as detailed in Sections 2.1.2 and 2.1.3. Code is available at https://github.com/CoAxLab/dynamic-hr.

Denoising constituted removal of physiological noise and motion artifacts (rotational and translational) from the hemodynamic signal itself. To do so, we used *niphlem* to generate variability regressors from the cardiac and respiratory response functions (Birn et al., 2008; Chang et al., 2009). We then conducted a GLM of these variability regressors onto our fMRI signal to capture the artifact components from mechanical physiological noise. We removed these artifacts from the fMRI signal by isolating the GLM residuals to use for further analysis.

The next stage of our pipeline was a leave-one-run-out nested cross-validated LASSO-PCA model that took the GLM residuals as input and predicted instantaneous heart period. We setup multiple models (13 total), each of which predicted instantaneous heart period from fMRI time series data at time points ranging from t-3 s to t+15 s (shifting by one TR at a time, i.e., 1.5 s). This range of lag time shifts between the fMRI signal and instantaneous

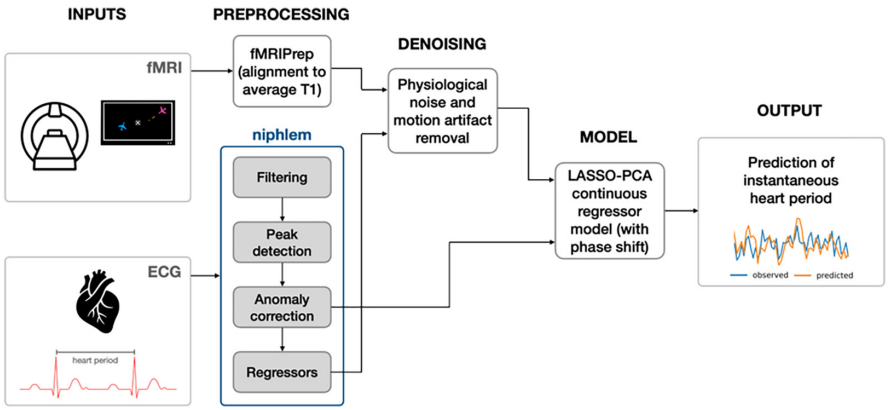

FIGURE 1 Analysis pipeline schematic.

heart period ensures that we take into account the HRF delay (6–8 s) inherent with BOLD data. See Figure 2b for a graphical illustration of the lag time shifts to isolate the desired drive signal. Thus, for each run across sessions, instantaneous heart period was predicted at every TR from GM voxels of the fMRI signal. First, as part of the PCA step, singular value decomposition was performed on the training runs to reduce the dimensionality of the predictor matrix. This also addresses the issue of multicollinearity across voxels. The inner loop then performed fivefold cross-validation on the training runs to optimize lambda (λ), the shrinkage parameter that controls the L1 penalty in LASSO, using a sequence of 100 λ values. Finally, the outer leave-one-run-out cross-validation loop performed the entire LASSO-PCA algorithm using this optimal lambda value. We repeated this analysis using the preprocessed time series before removal of artifacts for comparison.

Overall model performance was evaluated using prediction accuracy on a hold-out test set. This was done by comparing predicted heart period and observed heart period using fMRI runs that were not included in the model training. Model performance was measured using the Pearson correlation coefficient, r, between the heart period predicted from the brain responses and the observed heart period.

In order to visualize which brain regions were contributing the most to the prediction of heart period, we projected the voxelwise decoding maps into approximations of their encoding representations (Haufe et al., 2014). For this LASSO, coefficients were extracted from each model run and multiplied by the V matrix (from the singular value decomposition $X = USV^T$) to generate weights in feature space. These weights were then multiplied by the covariance matrix of X (our voxel data) to convert to encoding weights (Haufe et al., 2014).

To minimize computation time and excessive memory requirements of our analysis pipeline with large data sets, we adopted a modular approach that takes advantage of model averaging (Hoeting et al., 1999) (see Supplementary Materials and Figure S1 for further details). We trained individual LASSO-PCA models for each run and extracted the associated weights. For the outer leave-one-out cross-validation loop, we averaged these weights from the n-1-trained models, using the mean voxel decoding weights, to test our model's hold-out prediction accuracy.

We performed a two-sided one-sample $t$test on the encoding weights for lag time shift +7.5 s for each run with a false discovery rate (FDR) < 0.00005 to generate a statistically thresholded weight map corresponding to the Human QA dataset participant. This specific lag was chosen because it represents the optimal time point for detecting the blood oxygen level-dependent (BOLD) response evoked from underlying neural activity, given the sampling rate of the data set. Visualization of the participant's projected weights on the 3D brain was performed using Surf Ice (https://www.nitrc.org/projects/surfice/).

2.1.5 | Power analysis

We conducted a power analysis to test the number of runs needed for reliable prediction of heart period from fMRI data, using sample sizes $n = 2$, 4, 8, 10, 16, 20, and 30. For each sample size, we randomly selected n runs from the 42 total runs to use in our analysis. Working with the cleaned fMRI data at lag time shift +7.5 s, we trained a LASSO-PCA model on each run then used a leave-one-out

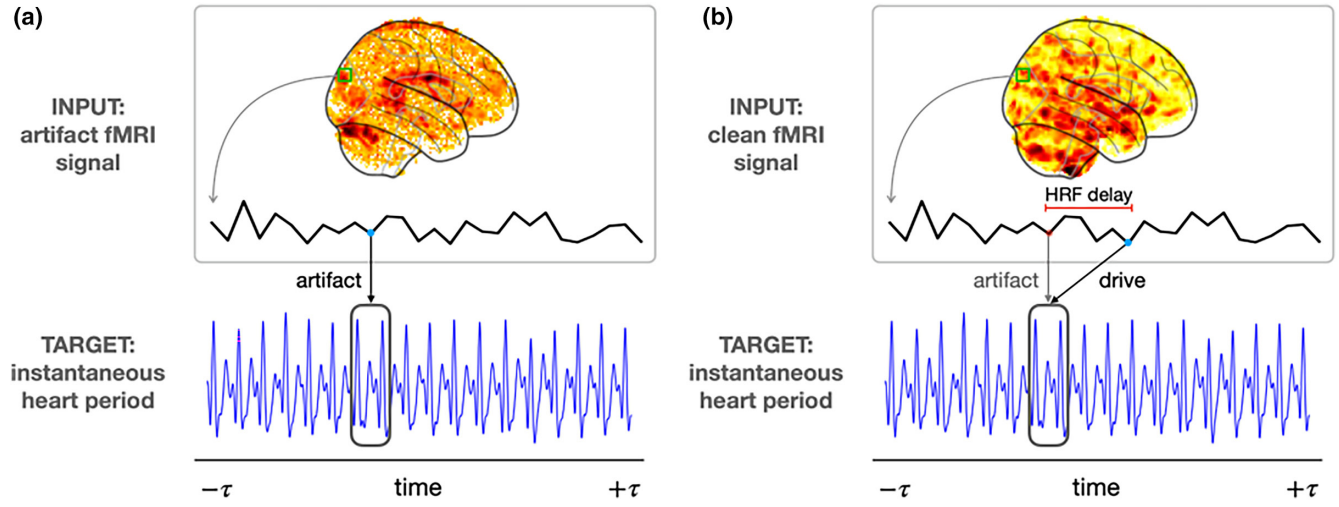

FIGURE 2 (a) Prediction of heart period from physiological noise component of fMRI signal. (b) Prediction of heart period after removing artifacts from the fMRI signal and accounting for the HRF delay.

cross-validation scheme to test each model on the average weights from the *n*-1-trained models, as described in Section 2.1.4. This procedure was repeated 40 times for each sample size. Hold-out test set prediction accuracy was evaluated using Pearson correlation coefficient and the mean *r* value and 95% confidence interval was calculated for each sample size.

2.2 | Natural scenes dataset (NSD)

2.2.1 | Participants

Neuroimaging and cardiovascular data from eight healthy participants (six females, two males; aged 19–32 years; three Asian, five White; BMI range: 17.5–25.2) from the NSD were used for Experiment 2. A detailed description of the Natural Scenes Dataset (NSD; http://naturalscenesdataset.org) is provided elsewhere (Allen et al., 2022). Physiological data was only available for a subset of scan sessions: four participants had data from 10 scan sessions (S1, S2, S5, and S7; nsd21–30), two participants had data from nine scan sessions (S3 and S6; nsd21–29) and two participants had data from seven scan sessions (S4 and S8; nsd21–27). Each session contained 14 functional runs (12 task and two resting-state scans). The total number of runs for each participant are as follows: S1 $n = 140$, S2 $n = 140$, S3 $n = 126$, S4 $n = 93$, S5 $n = 140$, S6 $n = 126$, S7 $n = 139$, and S8 $n = 84$.

2.2.2 | Heart period from pulse-oximetry

Physiological data from pulse-oximetry and pneumatic belt were used to record cardiac and respiration events, respectively. *Niphlem* was used as described in Section 2.1.2 to extract instantaneous heart period and generate cardiac and respiratory variability regressors. In this case, however, heart period was derived from the pulse-oximetry data.

Runs with noisy or interrupted pulse-oximetry data that prevented recovery of heart period were excluded from analysis: five runs for S4, one run for S7, and 14 runs (one entire session) for S8.

2.2.3 | MRI data acquisition and processing

Acquisition

FMRI data in the NSD were collected at 7T using a whole-brain, 1.8 mm, 1.6 s, gradient-echo, echo-planar imaging (EPI) pulse sequence. Resting-state and task-dependent functional images from a continuous visual recognition task were used. Further details can be found in (Allen et al., 2022).

Preprocessing

We used the 1.8 mm volume preparation of the preprocessed NSD time series data. FMRI preprocessing involved two steps. First, a temporal resampling was performed using a cubic interpolation. The time series for each voxel was upsampled to 1.333 s to correct for slice-time differences (resulting in 226 volumes for each run). Second, a spatial resampling was performed using a cubic interpolation to correct for head motion, EPI distortion, gradient nonlinearities, and across-scan-session alignment.

GM mask

We used the surface-based HCP_MMP1 parcellation (Glasser et al., 2016) available in 1.8 mm functional space for each participant to generate binary masks that limited our analyses to GM voxels.

2.2.4 | Individual participant analysis

Preprocessing, denoising, and model analyses for the NSD data were performed separately for each participant using the methods detailed in Section 2.1.4. We again setup 13 models in total, each of which predicted instantaneous heart period from fMRI time series data at time points ranging from *t*-2.66 s to *t* + 13.3 s (shifting by one TR at a time, i.e., 1.33 s).

We performed one-sampled, two-sided *t*tests on the encoding weights for lag time shift +7.99 s across runs for each participant with FDR < 0.05. For three participants, we were able to use more conservative thresholds: S3 = 0.0001, S5 = 0.005, and S7 = 0.001.

2.2.5 | Group analysis

We tested each participant's average trained model on every other participant for lag time shift +7.99 s. In order to do so, we first converted each participant's GM mask into MNI space (using the nsdcode mapping utility; https://pypi.org/project/nsdcode/) and then created a global participant mask from the union of the individual masks in MNI space. After converting the individual participant weight maps back into nifti images, we used the union MNI GM mask to extract matrices of a common size across participants. These weight matrices were averaged for each participant. Each average weight matrix was used as the trained model and tested on each individual run for every other participant, resulting in 56 group models. For each of these group models, we calculated the Euclidean

distance between weight maps as a measure of similarity. We also replicated the within-participant analysis in MNI space for lag time shift +7.99 s.

To visualize the common brain regions involved in prediction of heart period across participants, we generated two probability maps (one for positive weights and one for negative weights) that show the probability of a voxel being significant across participants. To do so, we thresholded and then binarized the positive and negative weights from the individual participant *t*tests separately, using FDR < 0.05. We then averaged the positive and negative weight maps separately across participants. Each voxel has a value between 0 and 1 that represents the probability of that voxel being significant across all participants. Positive and negative probability maps were overlaid and visualized using Surf Ice.

2.3 | Generalization

We conducted a cross-data set analysis to test the generalizability of our method and models, most notably across MRI acquisition resolutions. Using the NSD union MNI GM mask described in Section 2.2.5, we repeated the physiological denoising steps discussed in Section 2.1.4 on the Human QA dataset to extract the GLM residuals (X data) using an identical voxel mapping for both data sets. We then averaged the model decoding weights from lag time shift +7.99 s for all runs across all NSD participants to use as our average trained model. Finally, we tested each Human QA dataset run at lag time shift +7.5 s on the average NSD trained model, resulting in 42 total models. Model accuracy was again evaluated using Pearson correlation coefficient, along with mean and confidence interval summary measures.

3 | RESULTS

3.1 | Within-participant decoding performance

3.1.1 | Prediction of instantaneous heart period

Results for the single-participant data set from our leave-one-run-out cross-validation pipeline can be seen in

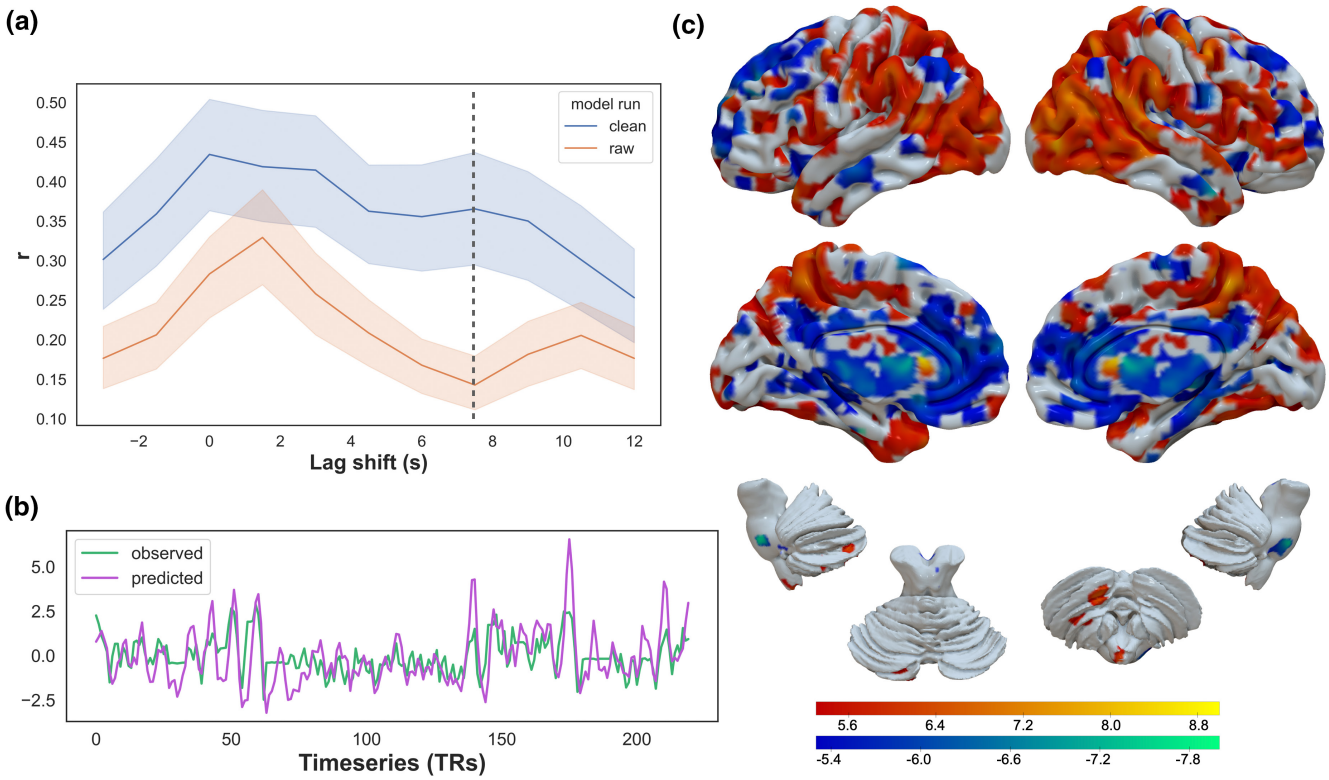

FIGURE 3 (a) Mean out-of-sample Pearson correlation coefficient, *r*, of predicted versus observed instantaneous heart period across 14 sessions (42 runs total) for each lag time shift for the original (orange) and cleaned (blue) fMRI signal. Shaded regions represent 95% confidence intervals (calculated using 1000 bootstrap iterations). Dashed vertical line represents the drive signal at lag time shift +7.5 s. (b) Example observed and predicted instantaneous heart period across the time series at time shift +7.5 s for a representative run. (c) One-sample *t*test (FDR correction <0.00005) of encoding weight maps of instantaneous heart period prediction across sessions and runs for the Human QA dataset participant at time shift +7.5 s. Positive weights are shown in red-yellow. Negative weights are shown in blue-green.

Figure 3. Here, we show our LASSO-PCA model prediction accuracy in the form of the correlation between observed and predicted heart period using clean, or denoised data (i.e., the residuals from the GLM of cardiac and respiration variability regressors), and the raw data (i.e., without the artifact signal from the physiological noise removed). When we look at how well our model predicts instantaneous heart period across lag time shifts, (Figure 3a), we see several patterns emerge. First, the cleaned data (blue lines), with the physiological noise artifacts removed, performs generally much better across lag time shifts than the raw data (orange lines), without the physiological artifacts removed (but otherwise identical). Second, we see the expected peak in prediction accuracy around the 0 and +1.5 s lag time shift, which reflects the point at which the physiological artifacts from cardiac and respiratory events would be expressed in the hemodynamic signal (see Figure 2a). Finally, there is an expected peak in model performance for the cleaned data, but not for the raw data, at lag time shift +7.5 s, as represented by the dashed vertical line in panel A, which accounts for any potential drive signals in the brain that regulate variation in instantaneous heart period. In particular, we only see this boost in model performance at this time shifted lag in the data where physiological artifacts have been removed from the signal. Figure 3b shows the instantaneous heart period time series from a single run in green, with the predicted heart period from the cleaned data model at lag time shift +7.5 s overlaid in purple. The close tracking of the predicted heart period time series with the observed instantaneous heart period visually demonstrates the peak in model performance associated with the brain's drive signal which regulates instantaneous heart period.

These results rely on a large, within-participant data set to predict instantaneous heart period from variations in the whole-brain hemodynamic signal (i.e., 42 fMRI runs collected across 14 separate sessions). One obvious question that arises is: is a data set this large necessary to predict instantaneous heart period within an individual? In order to determine the number of required runs needed for reliable prediction of heart period, we conducted a power analysis using sample sizes of $n = 2, 4, 8, 10, 16, 20$, and 30 runs at lag time shift +7.5 s. As shown in Figure S2, the correlation between observed and predicted heart period increases with increasing sample sizes, plateauing at approximately 16 runs, with a prediction accuracy of $r = 0.35$. However, the largest jump in prediction accuracy occurs when increasing from sample size of two runs to four runs, with a greater than 0.1 increase in Pearson correlation coefficient, r. Sample sizes greater than $n = 8$ show diminishing increases in prediction accuracy. Thus, it seems feasible to develop a reliable predictor of within-participant heart period variation from 1 to 2 sessions of fMRI scan time, without further optimization of the acquisition protocols (e.g., increased sampling rate and improved shimming).

3.1.2 | Areas that associate with instantaneous heart period

Now that we have shown it is possible to reliably predict heart period from whole-brain hemodynamic responses, we would like to know which areas are contributing to this prediction. Figure 3c shows the encoding maps, derived from the decoding weights, that reflect the brain regions that positively (red-yellow) and negatively (blue-green) associate with downstream changes in instantaneous heart period. Brain regions including the bilateral occipital cortex, superior parietal cortex, temporal pole, precuneus, supramarginal, dorsolateral prefrontal cortex (dlPFC), right insula, left cerebellum, and a portion of the left medial PFC (mPFC) were positively associated with heart period prediction. Specifically, for these regions, increases and or decreases in fMRI BOLD signal were associated with corresponding increased and or decreased instantaneous heart period. Bilateral occipital, superior parietal, supramarginal, temporal pole, superior temporal and temporoparietal junction appear to have the strongest positive association with heart period prediction. Comparatively, bilateral superior frontal, ventromedial PFC (vmPFC), middle temporal, anterior cingulate, angular gyrus, thalamus, and periaqueductal gray (PAG) regions were negatively associated with prediction of heart period. For these brain regions, there was an anticorrelated relationship between fMRI BOLD signal and instantaneous heart period, for example, an increase in the BOLD signal corresponded to a decrease in the instantaneous heart period. Bilateral anterior cingulate, middle temporal, left vmPFC, and right posterior cingulate seem to have the strongest negative association with heart period prediction.

3.2 | Across-participant performance

3.2.1 | Replicating single-participant results

In order to replicate our within-participant analysis and extend results to characterizing between-participant performance, we reran our model on the eight participants that make up the NSD (see Section 2.2.1). For this, we repeated the same analysis shown in Section 3.1 for each NSD participant across lag time shifts $-2.67\,\text{s} \leq t \leq 13.3\,\text{s}$ with the same LASSO-PCA method as used for the Human QA dataset. Figure 4a shows the individual model accuracies for each NSD participant as quantified by the

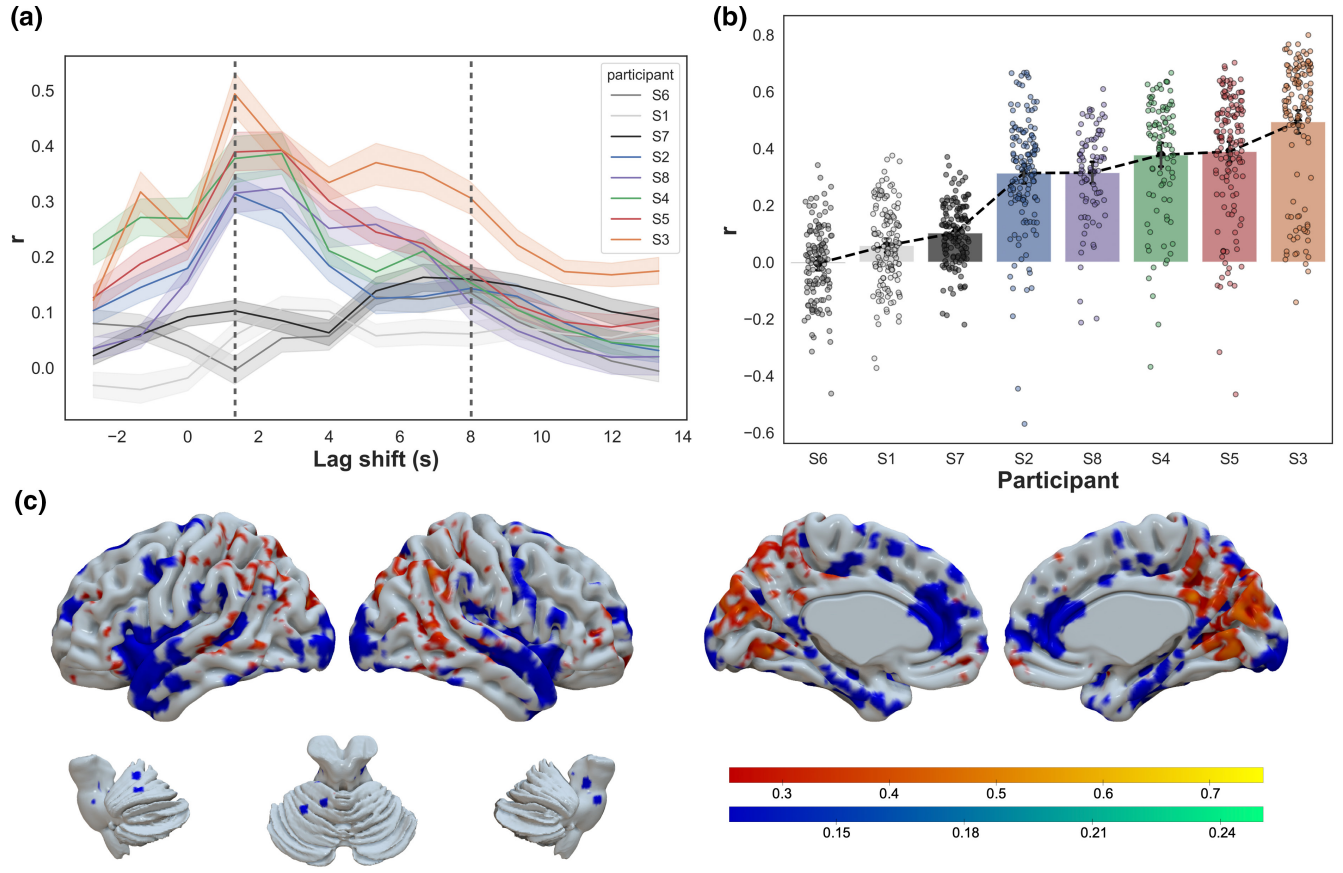

FIGURE 4 (a) Mean out-of-sample Pearson correlation coefficient, *r*, of instantaneous heart period for each participant for each lag time shift for the clean fMRI signal. Shaded regions represent 95% confidence intervals (calculated using 1000 bootstrap iterations). Dashed vertical lines represent the artifact signal (left) at leg time shift +1.33 s and the drive signal (right) at lag time shift +7.99 s. (b) Correlation coefficients for each run for each participant at lag time shift +1.33 s, reflected as the leftmost dashed line in panel A. Bars represent the mean *r* values; error bars show the 95% confidence intervals. (c) Probability map of encoding weights of instantaneous heart period prediction averaged across all participants at lag time shift +7.99 s. Positive weights are shown in red-yellow. Negative weights are shown in blue-green.

correlation between observed and predicted heart period across lag time shifts. We see an expected peak around lag time shift +1.33 s, as indicated by the leftmost dashed vertical line, that reflects the time window during which physiological artifacts manifest in the BOLD signal. Three participants (S1, S6, and S7), plotted in different shades of gray, have unexpectedly lower artifact signal correlation values (i.e., poor prediction at lag time shifts that should recover the physiological artifacts themselves). The rightmost dashed vertical line on the right at lag time shift +7.99 s represents the drive signal and is closest time point to the identified drive signal from the Human QA dataset at lag time shift +7.5 s. Focusing on how well the individual participant models predict instantaneous heart rate as part of the drive signal that regulates variation in heart period at lag time shift +7.99 s, we observed some variation across participants. The model accuracies for a majority of participants fall in the $0.15 \leq r \leq 0.2$ range (S2, S4–8), while S3 has a larger mean correlation value of $r = 0.3065$ and S1 has the smallest mean correlation value, of $r = 0.0609$. However, these patterns also persist across lag time shifts. It is also interesting to note that peak model performance associated with the drive signal does not appear to be located at lag time shift +7.99 s for most participants, and indeed the peak performance for NSD participants varies somewhat across time shifts. For example, for participants S3 and S8, the peak performance during the time window associated with the drive signal occurs at +5.33 s, while for S4 and S7, it occurs at +6.67 s. Additionally, participants S3, S4, and S8 have more obvious drive signal peaks than participants.

It is clear from Figure 4a that most, but not all, participants show reliable model performance. However, three participants appear to have overall low prediction accuracy, even in the baseline condition of predicting the time-window when the physiological artifacts are present. Figure 4b shows the prediction accuracy from the window that predicts the artifact signal, at lag time shift +1.33 s,

as shown by the leftmost dashed vertical line in panel A. For each participant (along the *x* axis), the correlation between observed and predicted heart period for every run is plotted as a separate point, while the bar shows the mean value and the error bars are 95% confidence intervals from 1000 bootstrap iterations. Participants are plotted in ascending order from left to right: S6 mean $r = -0.0044$, S1 mean $r = 0.0582$, S7 mean $r = 0.1028$, S2 mean $r = 0.3133$, S8 mean $r = 0.3147$, S4 mean $r = 0.3773$, S5 mean $r = 0.389$, and S3 mean $r = 0.4937$. Given the different artifact signal response for participants S1, S6, and S7, we might expect diminished results when generalizing to test across participants.

To see how well the pattern of encoding regions observed in the single-participant experiment (Section 3.1) replicates to a new data set, we performed the same encoding projection procedure in the NSD sample. Figure S3 shows these results for all participants except S6, for which no voxels survived correction at FDR < 0.05. For participants S3, S5, and S7, we used more conservative thresholds of FDR < 0.0001, 0.005, and 0.001, respectively. To visualize the common brain regions across participants, we performed a one-sample, two-sided *t*test using the average encoding weight maps for each participant. However, no voxels survived after correcting for multiple comparisons at a fairly liberal threshold, FDR < 0.05. Instead, we generated probability maps from the individual participant *t*tests that display the probability of a voxel surviving correction across all participants. Given the large percentage of voxels that are significant for at least one participant, 57%, Figure 4c shows only the voxels with a positive probability of 0.25 or greater, and voxels with a negative probability of 0.125 or greater. Brain regions along the bilateral medial wall and in the posterior cingulate and superior parietal areas were positively correlated with heart period prediction for at least two participants. Bilateral temporal pole, anterior cingulate, superior frontal and left cerebellum brain regions were negatively correlated with heart period prediction for at least one participant. Thus, we were largely able to replicate the cortical regions that regulate variation in instantaneous heart period. The variability in single trial encoding models, with strict corrections for multiple comparisons, is not surprising given the sample size used here, particularly since the goals of this study are prediction, not representational mapping.

3.2.2 | Generalization across participants

In order to see how well the decoding models work across participants, we tested generalization across the NSD participants, using the average trained model from one participant and testing it on every other participant. This allowed us to gauge the level of individual differences between decoding weight maps during the drive signal at +7.99 s. Figure 5a shows the average correlation between observed and predicted heart period for lag time shift +7.99 s for each training and testing participant combination of the group analysis. Darker colors represent lower prediction accuracy and lighter colors represent higher drive signal prediction accuracy. As anticipated, we are able to predict instantaneous heart period within participants more accurately than across participants, shown in the lighter colors along the diagonal and darker colors off the diagonal of Figure 5a. However, there are some exceptions for particular participants. Decoding weight maps for S8 predicted instantaneous heart period for S5 (mean $r = 0.1592$) more accurately than their own heart period signal (mean $r = 0.1215$). Similarly, S1 predicted S7 more accurately (mean $r = 0.1037$ compared to mean $r = 0.0572$). The horizontal and vertical white lines separate the participants with expected artifact signals (S2, S3, S4, S5, and S8) from those that behave somewhat as outliers (S1, S6, and S7), with either low or no peak in prediction accuracy during the artifact time window. Indeed as expected, when the decoding weight maps from these outlier participants are used as the training model, drive signal prediction accuracy performs more poorly in general, as shown in the darker colors of the lower left section of the heat map. Comparatively, it is interesting to note that when the outlier participants are used as test participants (upper right rectangle), model performance is generally higher. Focusing on the participant combinations in the top left rectangle, we show that generalization across participants is somewhat possible, albeit with lower performance. However, it is also clear that certain participant combinations have better model performance, which emphasizes the individual nature of the decoding weight maps that predict instantaneous heart period.

To get a clearer picture of this between-participant generalization, we plotted the within- and between-participant model accuracies separately in Figure 5b. Specifically, this compares the diagonal entries of the heat map (within-participant analysis) with the off-diagonal entries of the heat map (between-participant analysis), with gray dots representing a train-test participant combination that includes at least one outlier participant (S1, S6, and S7). The within-participant analyses have higher mean prediction accuracies (mean $r = 0.1588$) compared to the between-participant analysis (mean $r = 0.0570$). The outlier participant combinations have slightly lower mean prediction accuracies on average, though there is not a dramatic difference.

One factor that might explain this variability in between-participant prediction accuracy is the overall similarity in their decoding weight maps. In other words,

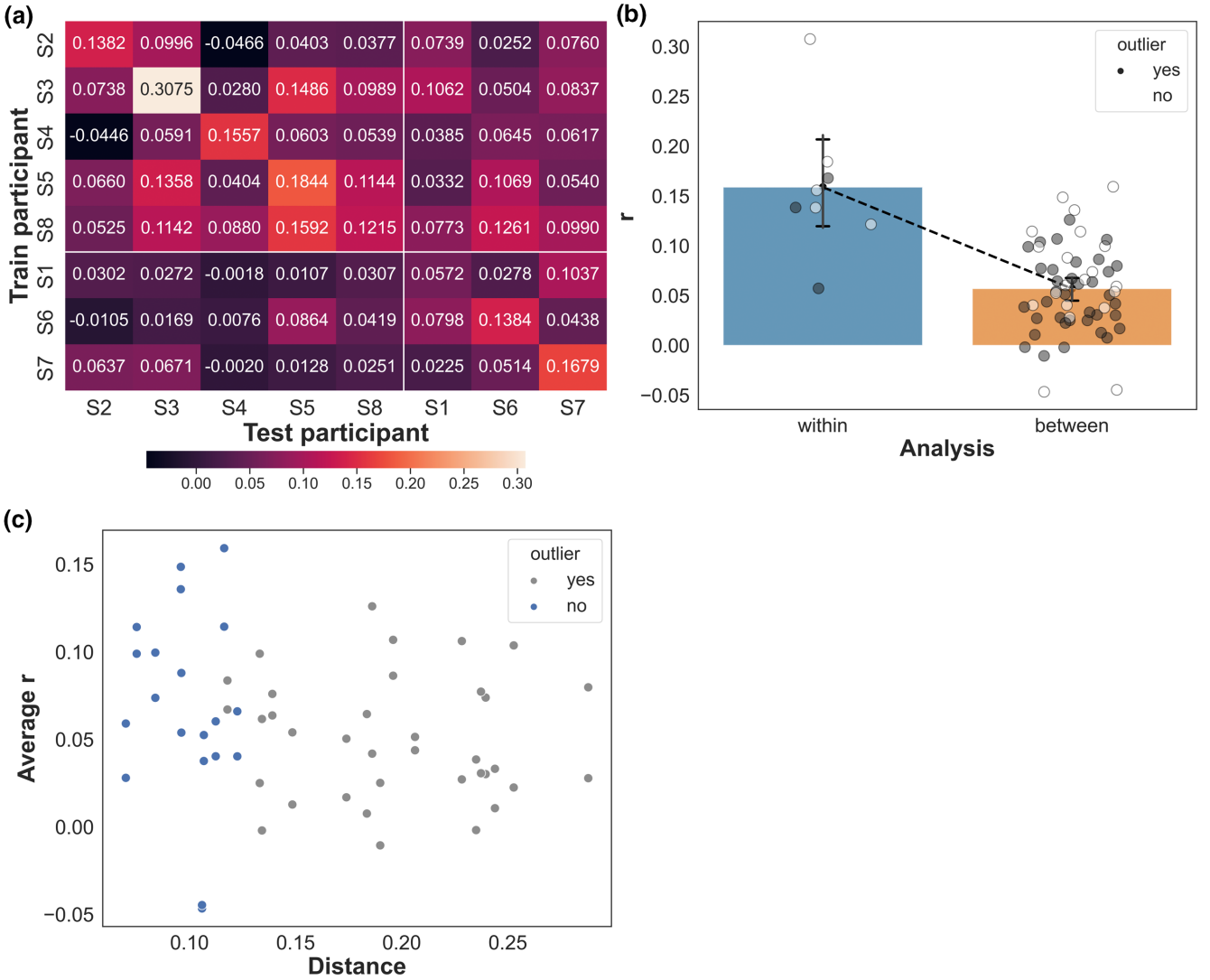

FIGURE 5 (a) Heat map of mean out-of-sample Pearson correlation coefficient values from the group analysis across participants at lag time shift +7.99 s, with training participants on the *y* axis and testing participants along the *x* axis. (b) Breakdown of within participant model *r* values (heat map diagonals) and across participant model *r* values (heat map off diagonals). Bars represent the mean *r* values; error bars show the 95% confidence intervals. Gray points indicate the presence of S1, S6, or S7 in the train-test participant combination. (c) Scatterplot of interparticipant Euclidean distance, on the *x* axis and the average decoding accuracy (*r* values) on the *y* axis for between participant models.

participants with more similar learned decoding models should also generalize better than pairs of participants with less similar models. To test this, we calculated the Euclidean distance between decoding weight maps for each pair of participants and then saw how well this distance was associated with the ability of one participant's model to predict the other's. As a way of visualizing the association between the similarity of different participant weight maps and the average prediction accuracy, we generated the scatterplot shown in Figure 5c. Each point represents a between-participant pair (e.g., S1–S2), with gray points again representing participant combinations that contain one or more outlier participants. While there is no significant relationship overall (Pearson $r = -0.2022$, 95% confidence interval [−0.4416, 0.0641]), it appears that the weight maps of participants that are not outliers are more similar than outlier participants, regardless of prediction accuracy. Thus, similarity in maps may correlate with the ability to generalize, but the current sample may be too small to discern a reliable statistical effect.

3.3 | Across scanner generalization

Finally, we set out to see how well decoding maps generated from one MRI scanner, in this case the 7T scanner, generalizes to data from another scanner (the 3T,

single-participant data set). We did this using the average NSD trained model (across all participants) and testing on the Human QA dataset runs for the drive signal time point (+7.99 s for NSD, +7.5 s for Human QA). This is a true generalization in that scanner strength, scan acquisition parameters and physiological recording methods were different across the two data sets. The correlation between observed and predicted heart period across runs ranged from $r = -0.0568$ to $r = 0.4040$, with a mean value of $r = 0.1424$ and 95% confidence interval [0.1058, 0.1775] (generated from 1000 bootstrap iterations), as shown in Figure 6. This demonstrates that our model is generalizable, though prediction accuracy is not as robust as in individual participant analysis.

4 | DISCUSSION

Being able to reliably estimate the neural control of cardiac function, within individuals, would present a first step in developing clinical biomarkers of brain contributions to CVD. Using machine learning approaches optimized for high-dimensional data sets, we successfully predicted instantaneous heart period from whole-brain hemodynamic data both within and across participants. We demonstrated these findings in two separate, highly sampled data sets that used different MRI and heart rate acquisition methods, as well as different fMRI parcellations. We first observed robust prediction accuracy of instantaneous heart period for single participants. The strength of this within-participant effect has to do with the high statistical power of predicting events across individual BOLD samples, as opposed to the trialwise or blockwise event-related designs of typical fMRI experiments. This allows for reliable prediction of individual participant effects. We have shown that only a handful of runs are needed for reliably predicting instantaneous heart period. Models are also modestly generalizable across individuals, though with marginally lower prediction accuracies than within-participant models. Finally, brain regions in the parietal, frontal, and temporal poles and in the anterior cingulate appear to reliably contribute to heart period prediction, suggesting that functional activity that is distributed across a network of cortical and subcortical brain regions relate to dynamic changes in heart period. Therefore, we have shown that dynamic fluctuations in the hemodynamic activity of brain areas implicated in the linkage of behavioral states to visceral control processes (e.g., [Eisenbarth et al., 2016; Wager et al., 2009; Zhang et al., 2023]) track with and predict transient fluctuations of heart period.

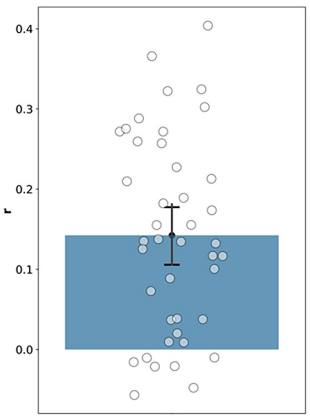

FIGURE 6 Correlation coefficient for each run from across scanner generalization models. The bar shows the mean *r* value; the error bars show the 95% confidence interval.

Despite the individual differences in brain regions associated with heart period prediction across participants in our study, taken together, the overlapping regions from both data sets are largely in line with existing literature. Eisenbarth et al. (2016), for example, demonstrated a multivariate pattern of social threat evoked fMRI activity that predicts heart rate (Eisenbarth et al., 2016). The positive predictive weights for this model were located in the dorsal anterior cingulate and negative predictive weights in the medial prefrontal cortex, which coincide with our results from both data sets. In addition, Gianaros et al. (2004) studied the associations between heart period and regional cerebral blood flow (rCBF) during a working memory task. Negative correlations between heart period and rCBF in the insula, anterior cingulate also align with results from both of our data sets (Gianaros et al., 2004). Similarly, Porro and colleagues (2003) also reported correlations between heart rate and fMRI activity during pain anticipation (Porro et al., 2003). Brain regions in the parietal cortex were positively correlated while regions in the medial prefrontal cortex and cingulate cortex were negatively correlated, which again overlap with our findings. Finally, Critchley et al. (2000) found associations with heart rate and rCBF during motor and arithmetic tasks (Critchley et al., 2000). Their negative correlations in the medial prefrontal and cingulate cortices with heart rate also coincide with our results. Altogether, these collective findings emphasize the relationship between specific cortical and subcortical brain regions that might regulate the chronotropic aspect of cardiac activity, and by extension cardiovascular risk. Where our results extend this prior work is in showing that not only are these critical brain regions in higher-level cortex (i.e., rostral to the brainstem) associated with cardiac function, but can reliably predict it on a moment-by-moment basis and at the single-participant level.

With this in mind, there are two main methodological limitations to consider when interpreting the results

of this study. First, there are temporal differences between the parasympathetic and sympathetic heart rate responses (Berntson et al., 1997) that we did not explicitly address in our analysis. Without the use of heart rate variability measures or systolic time intervals reflecting parasympathetic or sympathetic cardiac influences, we are unable to make strong or precise inferences about the autonomic neural correlates represented in our fMRI prediction maps. Intentionally incorporating more specific parasympathetic and sympathetic cardiac indicators into our predictive modeling pipelines would be a worthwhile future endeavor. Second, we treated task and rs-fMRI data identically, as the tasks from both data sets were not explicitly designed to evoke changes in heart rate, and any spontaneous changes in cardiac activity only increased usable variance for our models. It is still possible, however, that there are different brain processes across task-states that may have had some influence on the results and generalizability of our models. Indeed, one might expect increased prediction accuracy with increasing model complexity. An interesting first step in incorporating task data into our analyses would involve featurization of the images in the NSD visual recognition task to investigate whether heart period could be reliably predicted from the images themselves. Ultimately, our initial approach here was conservative in terms of maintaining a relatively simple model, without the added complexity that would be present when including additional task-based variables or parameters, while also providing some against information leakage. Follow-up work will explore this difference between situations where there may be more top-down control of cardiac function (e.g., tasks) from those where the system may be in a more passive state (e.g., rest).

Also, while our model predictions showed fairly high consistency at predicting heart period across participants, it is worth noting that the encoding maps showed substantial variability across cortical and subcortical regions as well. In some ways, this is not surprising. The decoding model used here was optimized for prediction, not localization, and uses correlated patterns across the entire brain to build its prediction. This can introduce substantial variability in the decoding weights, and consequently, the encoding projections used to localize regions of influence. Additionally, brainstem nuclei as well as the brainstem itself have specific anatomical characteristics that make neuroimaging data collection challenging and necessitate the use of high-field fMRI. These include size and shape of the nuclei themselves, proximity to large vessels, CSF and the oral cavity, as well as susceptibility to physiologic noise. 7T fMRI, with its capability for high spatial resolution and improved sign-to-noise ratios, has partially mitigated the effects of some of these obstacles. However, without focusing on specific brainstem nuclei ROIs or utilizing brainstem-specific processing methods (Mohamed et al., 2024), localization of brainstem regions associated with fMRI-autonomic correlations is limited. Our results in the 7T data set suggest that any questions on precise localization of control should rely on much larger data sets and specialized processing pipelines for 7T data where consistent patterns across individuals can be more reliably discerned.

Finally, it is important to keep in mind that our sample consisted of only healthy, young to midlife individuals. While the cardiovascular health of our sample was not directly tested, it is very likely that any cardiovascular disease risk in this sample is minimal. Thus, if we hope to translate the current approach to a meaningful measure of potential cardiovascular disease risk, follow-up work should investigate whether cortical control of heart period that we observe here persists in healthy older populations that often have higher risk of cardiovascular disease, as well as in populations with overt cardiovascular disease or other comorbidities. In order to make these translational steps, we must first prove that it is possible to measure the neural regulators of heart rate. This study provides this proof of concept that can be leveraged by future studies.

Despite these limitations, our study makes clear the feasibility of measuring the cortical and subcortical control signals, including brainstem areas, that are associated with variation in cardiac function in humans. To expand on the relevant immediate next steps, repeating our analysis with extended lag time shifts to look at predicting the sympathetic response and trying to tease out the distinction between the two responses could provide some additional nuances to our current results. It would also be valuable to examine any differences between the brain regions most important for parasympathetic versus sympathetic heart rate responses. Performing a simulated lesion analysis, by removing certain brain regions in turn, would be another method of evaluating the relative importance of individual brain regions (or networks) contributions. Finally, replicating this analysis on a much larger data sets, of hundreds or thousands of participants, would boost our ability to reliably localize consistent regions of control in the normative human brain. All these approaches reflect important next steps in our work.

5 | CONCLUSION

We have added to the growing existing body of literature looking at brain–heart connections, showing that heart period is reliably predicted by brain activity, even at the single-participant level, within cortical and subcortical

regions that are implicated in the visceral motor and visceral sensory control over cardiac activity. Ultimately, continued work to elucidate the role of the brain's cortical control mechanisms on cardiovascular function and disease risk is essential to further the development of novel therapies and prevention strategies for CVD.

AUTHOR CONTRIBUTIONS

Amy Isabella Sentis: Data curation; formal analysis; investigation; methodology; software; validation; visualization; writing – original draft; writing – review and editing. **Javier Rasero:** Data curation; formal analysis; resources; writing – review and editing. **Peter J. Gianaros:** Conceptualization; funding acquisition; project administration; supervision; writing – review and editing. **Timothy D. Verstynen:** Conceptualization; data curation; funding acquisition; investigation; methodology; project administration; resources; software; supervision; validation; visualization; writing – review and editing.

FUNDING INFORMATION

This work was supported by the National Institutes of Health T32GM008208-29, P01HL040962, and R01089850.

CONFLICT OF INTEREST STATEMENT

None.

DATA AVAILABILITY STATEMENT

The NSD is available at https://naturalscenesdataset.org/. The Human QA data are available from the corresponding author upon reasonable request.

ORCID

Amy Isabella Sentis https://orcid.org/0000-0003-3231-4322
Peter J. Gianaros https://orcid.org/0000-0003-2313-5277

REFERENCES

Allen, E. J., St-Yves, G., Wu, Y., Breedlove, J. L., Prince, J. S., Dowdle, L. T., Nau, M., Caron, B., Pestilli, F., Charest, I., Hutchinson, J. B., Naselaris, T., & Kay, K. (2022). A massive 7T fMRI dataset to bridge cognitive neuroscience and artificial intelligence. *Nature Neuroscience*, *25*, 116–126.

Berntson, G. G., Bigger, J. T., Jr., Eckberg, D. L., Grossman, P., Kaufmann, P. G., Malik, M., Nagaraja, H. N., Porges, S. W., Saul, J. P., Stone, P. H., & van der Molen, M. W. (1997). Heart rate variability: Origins, methods, and interpretive caveats. *Psychophysiology*, *34*, 623–648.

Berntson, G. G., Cacioppo, J. T., & Quigley, K. S. (1995). The metrics of cardiac chronotropism: Biometric perspectives. *Psychophysiology*, *32*, 162–171.

Birn, R. M., Smith, M. A., Jones, T. B., & Bandettini, P. A. (2008). The respiration response function: The temporal dynamics of fMRI signal fluctuations related to changes in respiration. *NeuroImage*, *40*, 644–654.

Böhm, M., Reil, J.-C., Deedwania, P., Kim, J. B., & Borer, J. S. (2015). Resting heart rate: Risk indicator and emerging risk factor in cardiovascular disease. *The American Journal of Medicine*, *128*, 219–228.

Boudoulas, K. D., Borer, J. S., & Boudoulas, H. (2015). Heart rate, life expectancy and the cardiovascular system: Therapeutic considerations. *Cardiology*, *132*, 199–212.

Brotman, D. J., Golden, S. H., & Wittstein, I. S. (2007). The cardiovascular toll of stress. *Lancet*, *370*, 1089–1100.

Carrive, P. (2006). Dual activation of cardiac sympathetic and parasympathetic components during conditioned fear to context in the rat. *Clinical and Experimental Pharmacology & Physiology*, *33*, 1251–1254.

Chang, C., Cunningham, J. P., & Glover, G. H. (2009). Influence of heart rate on the BOLD signal: The cardiac response function. *NeuroImage*, *44*, 857–869. https://doi.org/10.1016/j.neuroimage.2008.09.029

Critchley, H. D. (2005). Neural mechanisms of autonomic, affective, and cognitive integration. *The Journal of Comparative Neurology*, *493*, 154–166.

Critchley, H. D., Corfield, D. R., Chandler, M. P., Mathias, C. J., & Dolan, R. J. (2000). Cerebral correlates of autonomic cardiovascular arousal: A functional neuroimaging investigation in humans. *The Journal of Physiology*, *523 Pt 1*, 259–270.

Critchley, H. D., Mathias, C. J., Josephs, O., O'Doherty, J., Zanini, S., Dewar, B.-K., Cipolotti, L., Shallice, T., & Dolan, R. J. (2003). Human cingulate cortex and autonomic control: Converging neuroimaging and clinical evidence. *Brain*, *126*, 2139–2152.

Custodis, F., Schirmer, S. H., Baumhäkel, M., Heusch, G., Böhm, M., & Laufs, U. (2010). Vascular pathophysiology in response to increased heart rate. *Journal of the American College of Cardiology*, *56*, 1973–1983.

Dar, T., Radfar, A., Abohashem, S., Pitman, R. K., Tawakol, A., & Osborne, M. T. (2019). Psychosocial stress and cardiovascular disease. *Current Treatment Options in Cardiovascular Medicine*, *21*, 23.

de Geus, E. J. C., Gianaros, P. J., Brindle, R. C., Jennings, J. R., & Berntson, G. G. (2019). Should heart rate variability be "corrected" for heart rate? Biological, quantitative, and interpretive considerations. *Psychophysiology*, *56*, e13287.

Dimov, C. M., Anderson, J. R., Betts, S. A., & Bothell, D. (2020). A study on teamwork in a dynamic task. In Stewart T. C. ed. *Proceedings of ICCM 2019—17th International Conference on Cognitive Modeling*. Applied Cognitive Science Lab, Penn State. (pp. 47–52).

Eisenbarth, H., Chang, L. J., & Wager, T. D. (2016). Multivariate brain prediction of heart rate and skin conductance responses to social threat. *The Journal of Neuroscience*, *36*, 11987–11998.

Esteban, O., Markiewicz, C. J., Blair, R. W., Moodie, C. A., Isik, A. I., Erramuzpe, A., Kent, J. D., Goncalves, M., DuPre, E., Snyder, M., Oya, H., Ghosh, S. S., Wright, J., Durnez, J., Poldrack, R. A., & Gorgolewski, K. J. (2019). fMRIPrep: A robust preprocessing pipeline for functional MRI. *Nature Methods*, *16*, 111–116.

Fonov, V. S., Evans, A. C., McKinstry, R. C., Almli, C. R., & Collins, D. L. (2009). Unbiased nonlinear average age-appropriate brain templates from birth to adulthood. *NeuroImage*, *47*, S102.

Fox, K., Borer, J. S., Camm, A. J., Danchin, N., Ferrari, R., Lopez Sendon, J. L., Steg, P. G., Tardif, J. C., Tavazzi, L., & Tendera,

M. (2007). Resting heart rate in cardiovascular disease. *Journal of the American College of Cardiology*, *50*, 823–830.

Gianaros, P. J., Van Der Veen, F. M., & Jennings, J. R. (2004). Regional cerebral blood flow correlates with heart period and high-frequency heart period variability during working-memory tasks: Implications for the cortical and subcortical regulation of cardiac autonomic activity. *Psychophysiology*, *41*, 521–530.

Ginty, A. T., Kraynak, T. E., Fisher, J. P., & Gianaros, P. J. (2017). Cardiovascular and autonomic reactivity to psychological stress: Neurophysiological substrates and links to cardiovascular disease. *Autonomic Neuroscience*, *207*, 2–9.

Glasser, M. F., Coalson, T. S., Robinson, E. C., Hacker, C. D., Harwell, J., Yacoub, E., Ugurbil, K., Andersson, J., Beckmann, C. F., Jenkinson, M., Smith, S. M., & van Essen, D. C. (2016). A multi-modal parcellation of human cerebral cortex. *Nature*, *536*, 171–178.

Guyenet, P. G., & Koshiya, N. (1995). Working model of the sympathetic chemoreflex in rats. *Clinical and Experimental Hypertension*, *17*, 167–179.

Haufe, S., Meinecke, F., Görgen, K., Dähne, S., Haynes, J.-D., Blankertz, B., & Bießmann, F. (2014). On the interpretation of weight vectors of linear models in multivariate neuroimaging. *NeuroImage*, *87*, 96–110.

Hoeting, J. A., Madigan, D., Raftery, A. E., & Volinsky, C. T. (1999). Bayesian model averaging: A tutorial. *Statistical Science*, *14*, 382–401.

Huikuri, H. V., Jokinen, V., Syvänne, M., Nieminen, M. S., Airaksinen, K. E., Ikäheimo, M. J., Koistinen, J. M., Kauma, H., Kesäniemi, A. Y., Majahalme, S., Niemelä, K. O., & Frick, M. H. (1999). Heart rate variability and progression of coronary atherosclerosis. *Arteriosclerosis, Thrombosis, and Vascular Biology*, *19*, 1979–1985.

Jennings, J. R., Stringfellow, J. C., & Graham, M. (1974). A comparison of the statistical distributions of beat-by-beat heart rate and heart period. *Psychophysiology*, *11*, 207–210.

Jouven, X., Empana, J.-P., Schwartz, P. J., Desnos, M., Courbon, D., & Ducimetière, P. (2005). Heart-rate profile during exercise as a predictor of sudden death. *The New England Journal of Medicine*, *352*, 1951–1958.

Kivimäki, M., & Steptoe, A. (2018). Effects of stress on the development and progression of cardiovascular disease. *Nature Reviews. Cardiology*, *15*, 215–229.

Kraynak, T. E., Marsland, A. L., & Gianaros, P. J. (2018). Neural mechanisms linking emotion with cardiovascular disease. *Current Cardiology Reports*, *20*, 128.

Mohamed, A. Z., Kwiatek, R., Del Fante, P., Calhoun, V. D., Lagopoulos, J., & Shan, Z. Y. (2024). Functional MRI of the brainstem for assessing its autonomic functions: From imaging parameters and analysis to functional atlas. *Journal of Magnetic Resonance Imaging*. https://doi.org/10.1002/jmri.29286

Ongür, D., & Price, J. L. (2000). The organization of networks within the orbital and medial prefrontal cortex of rats, monkeys and humans. *Cerebral Cortex*, *10*, 206–219.

Palatini, P. (2007). Heart rate as an independent risk factor for cardiovascular disease: Current evidence and basic mechanisms. *Drugs*, *67 Suppl 2*, 3–13.

Palatini, P., & Julius, S. (1999). The physiological determinants and risk correlations of elevated heart rate. *American Journal of Hypertension*, *12*, 3S–8S.

Perret-Guillaume, C., Joly, L., & Benetos, A. (2009). Heart rate as a risk factor for cardiovascular disease. *Progress in Cardiovascular Diseases*, *52*, 6–10.

Porro, C. A., Cettolo, V., Francescato, M. P., & Baraldi, P. (2003). Functional activity mapping of the mesial hemispheric wall during anticipation of pain. *NeuroImage*, *19*, 1738–1747.

Steptoe, A., & Kivimäki, M. (2013). Stress and cardiovascular disease: An update on current knowledge. *Annual Review of Public Health*, *34*, 337–354.

Tawakol, A., Osborne, M. T., Wang, Y., Hammed, B., Tung, B., Patrich, T., Oberfeld, B., Ishai, A., Shin, L. M., Nahrendorf, M., Warner, E. T., Wasfy, J., Fayad, Z. A., Koenen, K., Ridker, P. M., Pitman, R. K., & Armstrong, K. A. (2019). Stress-associated neurobiological pathway linking socioeconomic disparities to cardiovascular disease. *Journal of the American College of Cardiology*, *73*, 3243–3255.

Thornton, J. M., Aziz, T., Schlugman, D., & Paterson, D. J. (2002). Electrical stimulation of the midbrain increases heart rate and arterial blood pressure in awake humans. *The Journal of Physiology*, *539*, 615–621.

Verberne, A. J. M., & Owens, N. C. (1998). Cortical modulation of the cardiovascular system. *Progress in Neurobiology*, *54*, 149–168.

Wager, T. D., Waugh, C. E., Lindquist, M., Noll, D. C., Fredrickson, B. L., & Taylor, S. F. (2009). Brain mediators of cardiovascular responses to social threat: Part I: Reciprocal dorsal and ventral sub-regions of the medial prefrontal cortex and heart-rate reactivity. *NeuroImage*, *47*, 821–835.

Zhang, J., Chen, D., Srirangarajan, T., Theriault, J., Kragel, P. A., Hartley, L., Lee, K. M., McVeigh, K., Wager, T. D., Wald, L. L., Satpute, A. B., Quigley, K. S., Whitfield-Gabrieli, S., Barrett, L. F., & Bianciardi, M. (2023). Cortical and subcortical mapping of the allostatic-interoceptive system in the human brain: Replication and extension with 7 tesla fMRI. bioRxiv. https://doi.org/10.1101/2023.07.20.548178

SUPPORTING INFORMATION

Additional supporting information can be found online in the Supporting Information section at the end of this article.

Data S1: Supporting Information.

How to cite this article: Sentis, A. I., Rasero, J., Gianaros, P. J., & Verstynen, T. D. (2024). Cortical and subcortical brain networks predict prevailing heart rate. *Psychophysiology*, *61*, e14641. https://doi.org/10.1111/psyp.14641